Article

Multi-Scale Computational Simulation of Amorphous Silicates. Structural, Dielectric and Vibrational Spectroscopic Properties

José Ángel Martínez-González [1,2], Javier Navarro-Ruiz [1,3] and Albert Rimola [1,*]

[1] Departament de Química, Universitat Autònoma de Barcelona, 08193 Bellaterra, Republic of Catalonia, Spain; joseangel.martinezg@gmail.com; jnavarro@iciq.es
[2] School of Biosystems and Food Engineering & School of Chemical & Bioprocess Engineering, University College Dublin, Belfield, Dublin, Ireland
[3] Institute of Chemical Research of Catalonia (ICIQ), Av. Països Catalans, 16, E-43007 Tarragona, Republic of Catalonia, Spain
* Correspondence: albert.rimola@uab.cat; Tel.: +34-935-812-164

Abstract: Silicates are among the most abundant and important inorganic materials, not only in the Earth's crust but also in the interstellar medium in the form of micro-/nano-particles or embedded in the matrices of comets, meteorites and other asteroidal bodies. Although the crystalline phases of silicates are indeed present in Nature, amorphous forms are also highly abundant. Here we report a theoretical investigation of the structural, dielectric and vibrational properties of the amorphous bulk for forsterite (Mg_2SiO_4) as a silicate test case by a combined approach of classical molecular dynamics (MD) simulations for structure evolution, and periodic quantum mechanical DFT calculations for electronic structure analysis. Using classical MD based on an empirical partial charge rigid ionic model within a melt-quenching scheme at different temperatures performed with the GULP 4.0 code amorphous bulk structures for Mg_2SiO_4 were generated using as initial guess the crystalline phase. This has been done for bulks with three different unit cell sizes adopting a super-cell approach; *i.e.*, 1×1×2, 2×1×2 and 2×2×2. The radial distribution functions indicated a good degree of amorphisation of the structures. Periodic B3LYP-geometry optimizations performed with the CRYSTAL14 code on the generated amorphous systems were used to analyze their structure, to calculate their high frequency dielectric constants (ε_∞), and to simulate the IR, Raman and reflectance spectra, which were compared with the experimental and theoretical crystalline Mg_2SiO_4. The most significant changes of the physico-chemical properties of the amorphous systems compared to the crystalline ones are presented and discussed (*e.g.*, larger deviations in the bond distances and angles, broadening of the IR bands, etc.), which are consistent with their disordered nature. It is also shown that by increasing the unit cell size the bulk structures present larger degree of amorphisation.

Keywords: DFT; periodic simulations; amorphous minerals, physico-chemical properties, super-cell

1. Introduction

Amorphous materials are disordered solid state systems that present a lack of long-range order and are thermodynamically less stable than their corresponding crystalline phases. However, despite the high degree of randomness of long-range structure, they possess a more regularity in their short-range structure, especially in the distribution of closest neighbors around each of the component units. As a consequence of lattice distortion, amorphous materials typically have different properties from their crystalline counterparts. This is the case, for instance, of silica [1].

Whereas crystalline silica manifests toxic effects in interaction with cellular systems [2–5], amorphous silica particles show high levels of biocompatibility [6], thus allowing them to be used in bioglass-based implants [7] and as drug delivery systems [8]. In other cases, because of the different physico-chemical properties between the crystalline and the amorphous partners, the amorphous phases are preferable to be used in semiconductor devices, such as the case of HfO_2 and ZrO_2 and their alloys [9–11].

The understanding and the prediction of the physico-chemical properties of non-crystalline solids rely on the proper description of their structure at the atomic level. Experimental techniques with this purpose are X-ray and neutron diffraction, which are directly sensitive to the structure, and also vibrational-related spectroscopies such as infrared (IR) and Raman, in which detailed structural information can be achieved. However, an atomic-level understanding of amorphous materials derived from these experimental methods has far remained elusive, in part because of the limited capabilities of the instrumentation for direct characterization. For instance, crystalline silicates exhibit a wealth of narrow IR bands [12,13], whereas for amorphous silicates these bands result in a significant broadening and blending due to the wide range of bond lengths and angles characteristic of the amorphous nature [14–16], Thus, deriving detailed structural information by means of these experimental techniques is a daunting task. A complimentary tool to obtain atomistic details of the structure of amorphous systems and its relationships with their physico-chemical features such as spectral signatures is the theoretical modeling approach. However, at variance with the crystalline systems, theoretical studies of the structure of amorphous materials are quite limited, probably because of the difficulty in generating realistic and reliable structural models with the available theoretical methods [17,18], Among the different strategies to generate bulk amorphous structures, the melt and quench scheme has successfully been used to simulate different amorphous oxides [11,18–26], This scheme consists of performing molecular dynamics (MD) simulations taking the crystalline bulks as initial guess and submitting them in a series of heating/cooling cycles. The heating at high temperatures followed by a rapid cooling allows sampling the large configurational spaces and ensures a good degree of amorphization of the initial crystalline systems. However, simulation of amorphous structures typically requires systems with more than 100 atoms. Accordingly, despite the enormous growth in computational power, generating highly disordered materials adopting the melt and quench scheme approach by means of first-principles MD simulations are often prohibitively expensive, so the simulation timescales are limited to several picoseconds, which are relatively short to evolve into the amorphous structures. As an alternative, classical force field MD simulations are computationally less expensive, thus allowing larger timescales up to several hundred picoseconds. By contrast, these classical MD simulations require accurate and reliable interatomic potentials, since the results are biased by the employed force fields. Proceeding this way, first-principles calculations onto the generated structural models are subsequently mandatory if electronic structure and spectroscopic properties are desired.

In this work, we combine classical MD simulations adopting the melt and quench scheme, for structural model generation, and DFT-based quantum mechanical (QM) calculations, for electronic structure analysis, to theoretically study the structural, electronic and spectroscopic properties of different amorphous silicate systems. Detailed analysis of the amorphous structures is carried out, including the coordination number and the radial distribution function of the systems. Geometry relaxations followed by calculation of the vibrational modes of the amorphous structural models serve to simulate the corresponding IR, Raman and reflectance spectra at the B3LYP density functional method by means of the periodic CRYSTAL14 *ab-initio* code [27], which in turn are compared with the corresponding crystalline systems and the available experimental data. Silicate-based materials constitute at *ca.* 95 percent of the rocks of the Earth's crust. Silicates form a class of inorganic materials with a large diversity in chemical composition and structural properties, in which the Si atoms are invariably tetrahedrally coordinated by four O atoms forming the orthosilicate $[SiO_4]^{4-}$ building block. The different silicate structures are produced by linking the corners of the individual $[SiO_4]^{4-}$ units with various levels of complexity. The negative net electrical charge is compensated by metal cations. The wide presence of silicates is not only limited to the

Earth's crust; they are also main components of the solid matter present in the Universe forming part in interstellar, circumstellar and interplanetary dust particles, comets, and meteorites [28–30]. The most astrophysically important silicate groups are olivines and pyroxenes, with the preponderance of Mg^{2+} and Fe^{2+} as countercations since they appear with the highest cosmic abundance. Olivines are characterized to have the $[SiO_4]^{4-}$ tetrahedra linked by Mg^{2+} and Fe^{2+} and general formula $Mg_{2x}Fe_{(2-2x)}SiO_4$ (x = 0 – 1), with the two end members named forsterite (Mg_2SiO_4) and fayalite (Fe_2SiO_4), whereas pyroxenes are formed by single chains of $[SiO_4]^{4-}$ intercalated by the divalent dications and have general formula $Mg_xFe_{(1-x)}SiO_3$ (x = 0 – 1) with the two end members named enstatite ($MgSiO_3$) and ferrosilite ($FeSiO_3$). At variance with the terrestrial silicates, cosmic silicates are mainly found in an amorphous state [28,31], probably due to their exposure to various processes during their life-cycle such as incidence cosmic rays and UV radiation, thermal shocks, or sputtering/shattering effects. Cosmic silicates play a significant role in the chemical evolution occurring in space as they provide the surfaces where important chemical reactions can take place, like the formation of H_2 [32] and H_2O [33,34]. This work focuses on the theoretical modelling and electronic structure study of amorphous Mg_2SiO_4. By matching the ab-initio results with the observational and experimental data, relationships between the molecular structure of dust and its physico-chemical features are elucidated.

2. Computational Methods

2.1. Classical Molecular Dynamics (MD) Simulations

The procedure to generate the amorphous silicate models is inspired with that done for simulate bioglasses [18,21,25]. All models were generated by means of classical molecular dynamics simulations using the atomistic Born model of solids [35] implemented in the General Utility Lattice (GULP) program [36]. This model represents all ions as point charges interacting through Coulomb forces. Pairwise Buckingham potentials were used to represent Pauli-repulsion and dispersion interactions, and the polarization of oxygen was represented by the shell model. All the interatomic potential parameters used in this work are shown in Table 1, which were derived from these references [37–39]. Moreover, the bulk structure of the crystalline Mg_2SiO_4 system calculated with GULP using these parameters is in very good agreement with the experimental one (see Figure S1 and Table S1 in supplementary material, SM). The classical molecular dynamics (MD) simulations were performed in the (N,V,T) canonical ensemble using the leapfrog Verlet algorithm with a 1 fs integration time step. The temperature control was achieved through velocity rescaling.

Table 1. Classical potential parameters used in this study.

Charges			
Ions	Core	Shell	Core-shell interactions (eVÅ^{-2})
Mg	+2.00000		
Si	+4.00000		
O	+0.84819	-2.84819	74.92

Buckingham Potential	A (eV)	ϱ (Å)	C (eV Å^6)
Mg_c-O_s	1428.500	0.31813	0.00000
Si_c-O_s	1283.907	0.32052	10.66158
O_c-O_s	22764.300	0.14900	27.88000

Threee-Body potential	k (eV rad^{-2})	Θ_0
O_s-Si_c-O_s	2.097240	109.47000

1) Nose-Hoover thermostat. A total of 17 different final temperatures were considered, between 400K and 2000K, separated by 100 K each. It is worth mentioning that higher temperatures than the melting point of Mg_2SiO_4 (at about 1800 K) would have been desirable to accelerate the

dynamic of the melting. However, we found that MD simulations at these temperatures (*e.g.*, 2500 K) the system was not stable because the interatomic potential parameters fail. After the heating process, classical MD simulations at the (N,V,T) ensemble, at the given temperature, were performed, which consisted of a 100 ps equilibration phase and a 200 ps production phase.

2) Cooling phase: After the production phase of the previous step, the resulting systems were subjected to MD simulations where the temperature was decreased by 0.005 K every time-step to reach the temperature of 300K. At this temperature, the systems were equilibrated during 50 ps.
3) Second Thermal/Production: The structures obtained after the cooling simulations were then heated again to the temperature chosen in the first step. Then, MD simulations with an equilibration phase of 100 ps and a production phase of 200 ps production were performed.

2.2. Quantum Mechanical (QM) Calculations

The resulting amorphous structures generated by the classical MD simulations were then optimized by means of periodic quantum mechanical calculations. All these calculations were performed with the periodic ab initio CRYSTAL14 code [27]. This code implements the Hartree–Fock and Kohn–Sham self-consistent field method based on localized Gaussian Type Orbitals (GTO) for periodic systems.

The multielectron wave function is described by linear combination of crystalline orbitals, which in turn are expanded in terms of GTO basis sets. Specifically, oxygen, magnesium, silicon, and iron were described by (8s)-(411sp)-(1d), (8s)-(511sp)-(1d), (8s)-(6311sp)-(1d), and (8s)-(64111sp)-(1d) contractions, respectively. All the SCF calculations and geometry optimizations were performed with the B3LYP [40,41] density functional method. Geometry optimizations have been performed in P1 group symmetry (no symmetry), in order to ensure the maximum degrees of freedom during the optimization. Both lattice constants and internal coordinates have been simultaneously optimized within the same run, using analytical gradients and upgrading the numerical Hessian with the Broyden–Fletcher–Goldfarb–Shanno (BFGS) algorithm [42]. These methods were already used in previous works focused on the crystalline forsterite [43–45] and fayalite bulk properties [46].

Default values of the tolerances that control the Coulomb (6 6) and exchange (6 6 16) series have been adopted. This means that when the overlap between two atomic orbitals is smaller than 10^{-6} (for Coulomb) and 10^{-16} (for exchange) the integral is either approximated or disregarded. The Hamiltonian matrix has been diagonalized in 63 reciprocal lattice points (k points) to sample the Brillouin zone, corresponding to a shrinking factor of 5 [47]. Open-shell calculations were based on an unrestricted formalism.

Phonon frequencies of the considered systems have been calculated as the eigenvalues obtained by diagonalizing the mass-weighted Hessian matrix at Γ point (point $k = 0$ in the first Brillouin zone, called the central zone). The mass-weighted Hessian matrix was obtained by numerical differentiation (central-difference formula) of the analytical first energy derivatives, calculated at geometries obtained by displacing, in turn, each of the 3N equilibrium nuclear coordinates by a small amount, $u = 0.003$ Å. We refer to this work [48] for a complete discussion of the computational conditions and other numerical aspects concerning the calculation of the vibrational frequencies at the Γ point. The value of the infrared intensity for each normal mode was also computed via the dipole moment variation along the normal mode adopting the set of localized Wannier functions [49–51], whereas Raman intensities were calculated analytically through the coupled-perturbed Hartree-Fock (CPHF) scheme implemented in CRYSTAL [52,53] and successfully performed for different crystalline minerals [54–62]. Reflectance spectra ($R(\nu)$) of the silicate systems were simulated by combining different ingredients available in the code: i) calculation of the vibrational modes, their corresponding intensities, and separation of the transverse and longitudinal optical (TO and LO, respectively) modes [48, 63], ii) calculation of the high frequency dielectric tensor (ε_∞) (ref. [58–61]) contributing to the frequency-dependent complex dielectric function ($\varepsilon(\nu)$) [52,53,64,65], and iii) calculation of the mass-weighted effective mode Born charges [66–68]. Reflectance spectra of several crystalline mineral systems have successfully been simulated [44–46, 69–71].

Peer-reviewed version available at Minerals 2018, 8, 353; doi:10.3390/min8080353

3. Results and Discussion

This section is organized as follows. The first part addresses the generation of an amorphous structure of forsterite (Mg_2SiO_4) bulk by means of classical MD simulations and subsequently optimized at a quantum chemical level. A structural analysis of the optimized structure is presented and investigations on its dielectric and vibrational properties by calculating the high frequency dielectric constants and simulating the infrared, Raman and reflectance spectra are shown, which in turn are compared with the experimental and theoretical crystalline Mg_2SiO_4 data. The second part is focused on the influence of the unit cell size of the amorphous Mg_2SiO_4 bulk on the structural, dielectric and vibrational properties.

3.1. The Amorphous 1×1×2 Super-Cell Mg_2SiO_4 System

As mentioned in Computational Methods, the initial guess to generate the amorphous Mg_2SiO_4 bulk structure (hereafter referred to as Fo) was the Mg_2SiO_4 crystalline system. The bulk crystal structure of Mg_2SiO_4 consists of distorted SiO_4 tetrahedra and MgO_6 octahedra, in which the tetrahedra and octahedra share the vertices (see Figure 1). Half of the available octahedral voids are occupied by the divalent cations. This crystal system has two symmetry-independent Mg atoms, named Mg1 and Mg2. The Mg1-centered octahedra share edges forming rods parallel to the crystallographic c axis, and the Mg2 octahedra are laterally linked to these rods through the corresponding edges (shown in Figure 1).

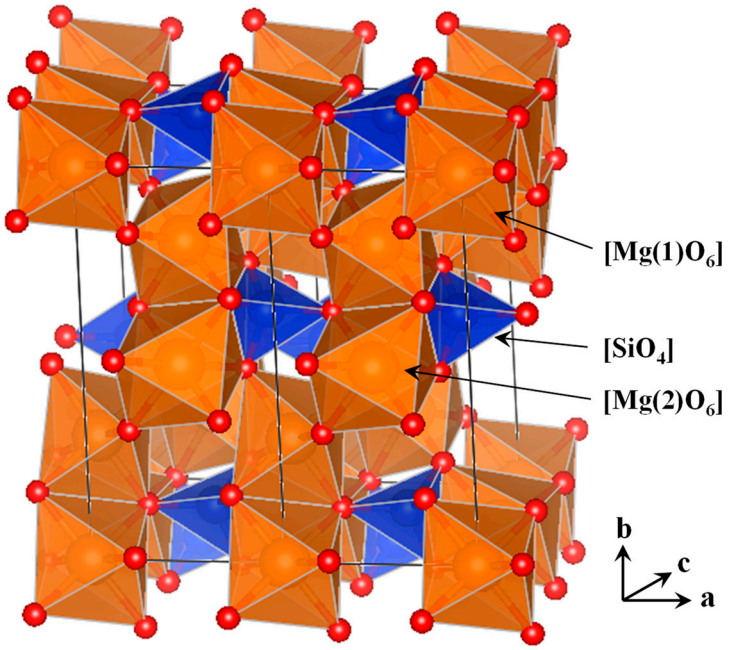

Figure 1. View (along the *c* crystallographic axis) of the crystal structure of forsterite. The two symmetry-independent Mg atoms are indicated according to the octahedral units [Mg(1)O_6] and [Mg(2)O_6] (in brown). The tetrahedral [SiO_4] unit blocks (in blue) are also indicated. O atoms are in red.

Classical MD simulations at different temperatures adopting the procedure described in Computational Methods were executed to amorphize the structure of crystalline Mg_2SiO_4. As the unit cell is relatively small (*Pbnm* space symmetry with lattice parameters of a = 4.79 Å, b = 10.19 Å, and c = 5.85 Å), in this part, a larger unit cell has been adopted by doubling the c lattice parameter to favor an easier amorphization of the structure (hereafter referred to as 1×1×2). In the next section, a detailed analysis of the effect of the unit cell size in the physico-chemical properties of the amorphous structures is presented. Figure 2 shows the resulting structures at the end of the classical MD simulations run at the different temperatures. As one can see, the initial crystallinity becomes

lost when increasing the temperatures. Figure 3 shows the pair-correlation functions, $g(r)$, for the Mg atoms with either the neighboring Mg atoms (a, Mg-Mg) or the O atoms (b, Mg-O) derived from the classical MD simulations at T = 300, 700, 900, 1200, 1500, and 1800 K. At 300 K, the $g(r)$ functions present a first sharp peak, followed by a subset of lower well-defined peaks, in agreement with the crystalline nature of Fo at this temperature. The first peak is representative of the Mg-Mg and Mg-O lengths of the first shell, while the others represent the distribution of the Mg-Mg and Mg-O distances of the outer shells. An increase of the temperature produces a broader profile of $g(r)$, in which the first peak loses significantly the intensity while the others overlap each other up to a point where at high temperatures only two broad peaks are appreciable. These changes clearly indicate that a progressive loss of crystallinity occurs upon temperature increase.

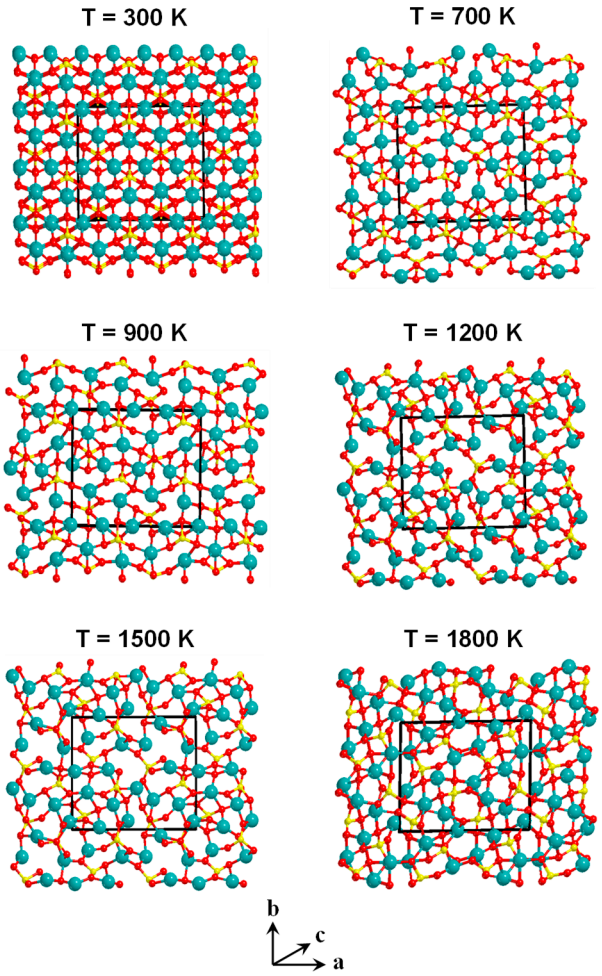

Figure 2. Structures obtained by classical molecular dynamics (MD) simulations. For all simulations, the initial guess structure was the crystal system. It was initially heated up to the given temperature and then submitted to the MD simulations at the (N,V,T) ensemble. Unit cells are shown in black.

Preprints (www.preprints.org) | NOT PEER-REVIEWED | Posted: 26 June 2018 doi:10.20944/preprints201806.0423.v1

Peer-reviewed version available at Minerals 2018, 8, 353; doi:10.3390/min8080353

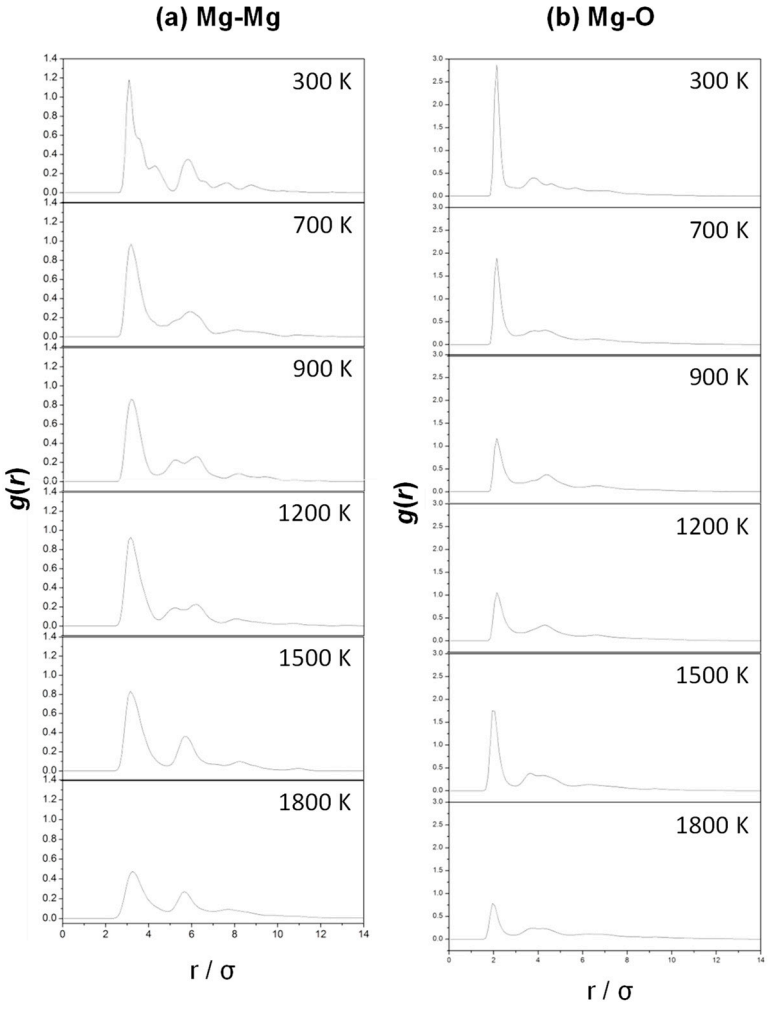

Figure 3. Mg-Mg (a) and Mg-O (b) pair correlation functions derived from the MD simulations ate the different temperatures.

As the structure generated at T = 1800 K is the most disordered one, this was chosen to study at the DFT level the structural and vibrational properties. Figure 4 shows the initial (crystalline) and the final (amorphous) structures optimized at the B3LYP theory level. It is also worth mentioning that those structures generated between 400 and 1600 K collapsed onto the crystal system upon optimization, whereas those between 1700 and 2000 K remained as amorphous structures. Table 2 shows the B3LYP-optimized lattice parameters and the range of the calculated Mg-O and Si-O bond lengths of amorphous Fo, as well as the volume and the density. For comparison, Table 2 also presents the same parameters for Fo crystal (experimental and calculated). In addition to the systematic larger values provided by the calculated values for the crystal system, results indicate that the range of values of the amorphous system is larger than the crystal ones. This is indicative that the B3LYP-optimized amorphous Fo presents a larger distribution of bond lengths characteristic of the amorphous materials. It is worth mentioning that due to the disorganization of the internal atomic positions in the amorphous Fo, classifying the Mg atoms in Mg1 and Mg2 is not possible. The cell parameters of the amorphous Fo experiencing more variation compared to the crystalline values are *a* and *b*; *i.e.*, the former is about 0.2 Å larger while the later 0.8 Å shorter. Calculated lattice angles are also somewhat different, which essentially deviate of the ideal 90 degrees. Because of the significant shortening of the *b* cell parameter, the volume of the amorphous Fo is smaller than the crystal volumes. The fact that the density of the crystalline systems is higher than the amorphous one is also indicative of the amorphisation of the system. Indeed, bearing in mind that amorphous

materials are characterized by a random structure and poor order giving rise to the presence of porous, the density of amorphous materials is lower than the crystalline analogues.

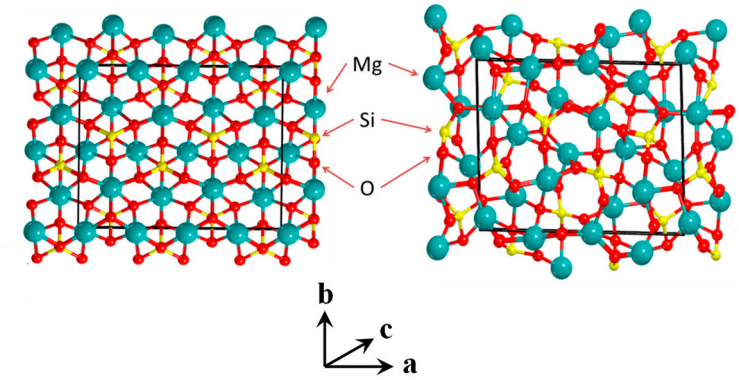

Figure 4. B3LYP-optimized structures of the bulk structure of Mg_2SiO_4 in the crystal form (left) and in an amorphous form generated by classical MD simulations at T = 1800 K. Unit cells are shown in black.

Table 2. Cell parameters and bond distance ranges of the Mg_2SiO_4 bulk structures: experimental values of the crystal system and B3LYP-optimized values of the crystal and amorphous systems. Calculated volume and densities derived from the B3LYP-optimized geometries are also shown.

	experimental	crystal	amorphous
Si-O (Å)	1.616 – 1.649	1.628 – 1.673	1.618 – 1.693
Mg1-O (Å)	2.069 – 2.126	2.073 – 2.131	1.929 – 2.226
Mg2-O (Å)	2.040 – 2.166	2.062 – 2.222	–
a (Å)	4.746	4.789	4.93
b (Å)	10.18	10.25	9.37
c (Å)	5.976	6.009	5.97 (11.94) [1]
α (degrees)	90.0	90.0	87.4
β (degrees)	90.0	90.0	90.6
γ (degrees)	90.0	90.0	88.6
Volume (Å^3)	288.73	295.10	275.78 (551.00) [1]
Density (g cm^{-3})	3.22	3.34	3.373

[1] Because of the enlargement of the unit cell along the *c* axis (see text), for a proper comparison, bare values were derived from the actual calculated values (values in parenthesis).

In order to understand the nature of the amorphisation of the silicate material, we examined the deviation of the internal O-Si-O and O-Mg-O angles of the optimized system with respect to the ideal values (reported in Table 3). These values reveal that the O-Mg-O angle presents the largest deviation (≈ 15.3 %) and therefore the distortion of these angles contributes significantly to the amorphous nature. However, the deviation of the O-Si-O angle is not contemptible (≈ 6.5 %) so the distortion of these angles also contributes by some amount to the internal atomic disorder.

The high frequency dielectric constants (ε_∞) were also calculated using the CPKS scheme implemented in the CRYSTAL code. Results are shown in Table 4, in which the ε_∞ values along the *x*, *y* and *z* direction of the amorphous Fo are compared with the experimental and calculated ones for Fo crystal. For the crystal systems ε_∞ is notably symmetric, the values slightly differing as a function of the direction; *i.e.*, both experimental [72] and calculated values give $\varepsilon_{\infty,x}$ as the largest value whereas the shortest on $\varepsilon_{\infty,y}$, with a difference of 0.12 – 0.15 units. In contrast, for amorphous Fo, the difference between the largest and the smallest ε_∞ values, which now correspond to $\varepsilon_{\infty,x}$ and $\varepsilon_{\infty,z}$, respectively, is a meager 0.07 units. This is consistent with the disordered nature of amorphous Fo, since the direction-dependency of ε_∞ usual in crystalline systems is partially lost.

Table 3. Mean values and the corresponding average deviations (with respect to the ideal value) of the O-Si-O and O-Mg-O angles of the optimized amorphous 1×1×2, 2×1×2 and 2×2×2 Mg_2SiO_4 systems.

Angle (degrees)	Ideal value	Mean value ± standard deviation [average deviation]		
		1×1×2	2×1×2	2×2×2
O-Si-O	110.0	109.5 ± 7.2 [6.53 %]	108.9 ± 12.4 [11.3 %]	104.9 ± 12.8 [11.6 %]
O-Mg-O	90.0	94.7 ± 13.8 [15.3 %]	100.9 ± 22.1 [24.6 %]	104.1 ± 16.5 [18.3 %]

Table 4. High frequency dielectric constants (ε_∞) for the Mg_2SiO_4 bulk structures along the x, y and z directions: experimental values of the crystal system and B3LYP-optimized values of the crystal and amorphous systems.

	Experimental [1]	crystal	amorphous
$\varepsilon_{\infty,x}$	2.789	2.571	2.284
$\varepsilon_{\infty,y}$	2.673	2.424	2.247
$\varepsilon_{\infty,z}$	2.726	2.475	2.218

[1] From ref. [72]

Crystalline Fo has an orthorhombic structure. It presents 28 atoms in the unit cell (six symmetry-independent atoms), which give rise to four formula units per cell. Their symmetry decomposition corresponds to $\Gamma_{total} = 11A_g + 11B_{1g} + 7B_{2g} + 7B_{3g} + 10A_u + 10B_{1u} + 14B_{2u} + 14B_{3u}$, in which the three B_{1u}, B_{2u} and B_{3u} correspond to rigid transitions and the remaining modes are vibrations that can be classified as: 35 IR active modes ($9B_{1u} + 13B_{2u} + 13B_{3u}$), 36 Raman active modes ($11A_g + 11B_{1g} + 7B_{2g} + 7B_{3g}$), and $10A_u$ inactive modes. In previous works, mode classification and band assignments of crystaline Fo have exhaustively been discussed by means of infrared, Raman, and reflectance spectroscopic measurements [13, 73–80]. In this part, we focus our attention on the most important changes due to the amorphisation of the crystal system. Figure 5 shows the B3LYP-simulated IR spectrum of amorphous Fo (a), where for comparison, the B3LYP-simulated (b) and the experimental (c) IR spectra for the crystal systems are also shown. The simulated spectra were broadened by Lorentzian functions with a typical width $\delta\nu = 20$ cm^{-1}, which is comparable with the bandwidth of the experimental IR spectrum. For crystal Fo, the experimental and theoretical vibrational IR and Raman spectra compare fairly well. In the IR case, both spectra present a wealth of narrow bands in agreement with their crystalline nature. As already described by some of us and by other colleagues, B3LYP frequencies reproduce very well the experimental IR values (for more details see ref. [43,81]). Figure 6 shows the B3LYP-simulated Raman spectrum of amorphous (a) and crystal (b) Fo and Table 5 reports the calculated Raman active frequencies (classified by their symmetry) with the corresponding intensity of the crystalline system, which are compared with those measured experimentally (including frequency deviations). In the Raman case, B3LYP reproduces quite well the experimental Raman data, with a mean average deviation of 24.9 – 34.6 cm^{-1} and a largest deviation of 81 – 82 cm^{-1}. Remarkably, for the calculated two most intense Raman peaks (*i.e.*, at 848 and 883 cm^{-1}) the deviations compared to the corresponding experimental values are of 27 and 22 – 24 cm^{-1}.

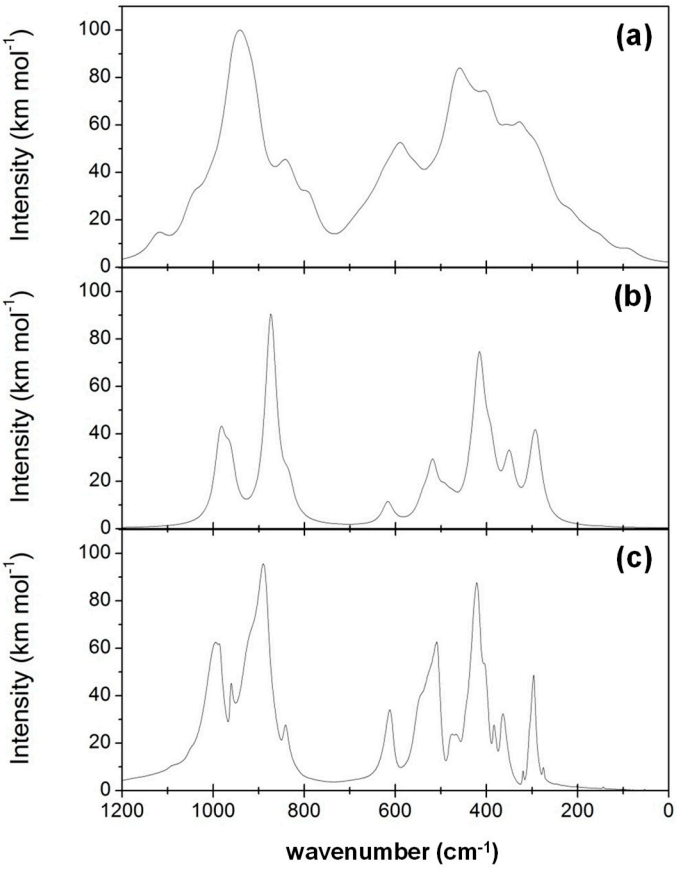

306 **Figure 5.** B3LYP-simulated IR spectra of the amorphous (a) and crystalline forsterite (b). The
307 experimental spectrum of the crystalline forsterite is also included (c).

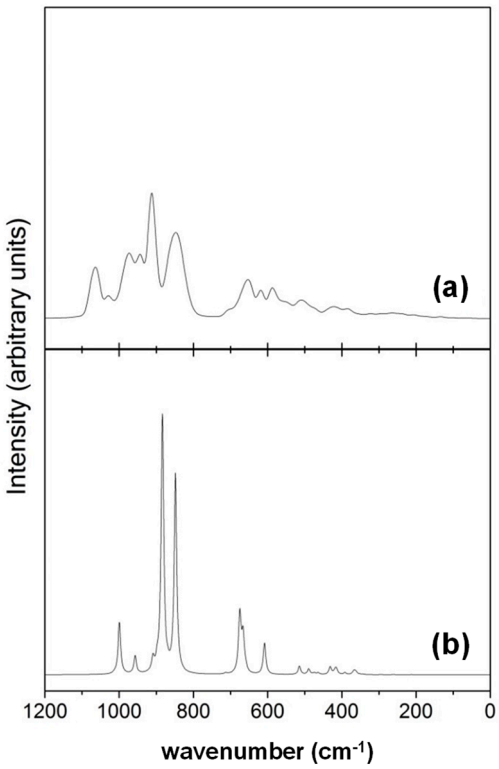

308 **Figure 6.** B3LYP-simulated Raman spectra of the amorphous (a) and crystalline forsterite (b).

Preprints (www.preprints.org) | NOT PEER-REVIEWED | Posted: 26 June 2018 doi:10.20944/preprints201806.0423.v1

Peer-reviewed version available at Minerals 2018, 8, 353; doi:10.3390/min8080353

Table 5. Active Raman frequencies (ν, in cm^{-1}) calculated in this work and their comparison with the experimental data. The shifts between the calculated and the experimental values ($\Delta\nu$) are also provided.

	N	This work		Ref. [77]		Ref. [75]		Ref. [74]		Ref. [73]	
		ν	I (%)	ν	Δν	ν	Δν	ν	Δν	ν	Δν
A_g	1	212	0.05	184	28	183	29	183	29	183	29
	2	261	0.08	227	34	226	35	227	34	227	34
	3	351	0.11	304	47	304	47	305	46	305	46
	4	367	1.20	329	38	329	38	329	38	329	38
	5	391	0.78	339	52	332	59	340	51	340	51
	6	474	0.62	421	53	422	52	424	50	424	50
	7	608	12.4	544	64	545	63	546	62	545	63
	8	675	22.2	608	67	608	67	609	66	609	66
	9	848	81.1	824	24	824	24	826	22	826	22
	10	883	100	856	27	856	27	856	27	856	27
	11	999	20.6	966	33	965	34	966	33	966	33
B_{1g}	12	253	0.00	-	-	220	33	224	29	197	56
	13	294	0.06	-	-	274	20	260	34	265	29
	14	361	1.05	316	45	318	43	318	43	317	44
	15	417	1.68	-	-	351	66	-	-	-	-
	16	420	0.38	-	-	383	37	418	2	418	2
	17	489	2.21	434	55	434	55	434	55	434	55
	18	658	1.39	588	70	582	76	585	73	583	75
	19	713	0.43	-	-	632	81	632	81	632	81
	20	869	1.28	838	31	838	31	839	30	839	30
	21	897	3.37	866	31	866	31	866	31	866	31
	22	1012	0.37	-	-	975	37	976	36	976	36
B_{2g}	23	-		-	-	175	-	142	-	-	-
	24	229	0.01	243	-14	242	-13	244	-15	244	-15
	25	343	0.17	-	-	323	20	324	19	324	19
	26	365	0.08	-	-	365	0	368	-3	365	0
	27	431	2.93	-	-	-	-	-	-	407	24
	28	463	0.69	434	29	439	24	441	22	438	25
	29	665	14.3	588	77	586	79	588	77	585	80
	30	956	6.98	882	74	881	75	884	72	881	75
B_{3g}	31	203	0.00	243	-40	-	-	226	-23	-	-
	32	296	0.00	-	-	286	10	272	24	-	-
	33	-		316	-	315	-	318	-	314	-
	34	369	0.31	373	-4	374	-5	376	-7	374	-5
	35	413	1.35	409	4	410	3	412	1	406	7
	36	-		-	-	435	-	-	-	466	-
	37	514	3.34	-	-	-	-	-	-	484	30
	38	670	2.82	588	82	592	78	595	75	591	79
	39	908	5.14	920	-12	920	-12	922	-14	920	-12

More interesting are the differences between the B3LYP-simulated crystalline and amorphous IR and Raman spectra. Crystal Fo presents a set of well-defined bands, in which the total active vibrations are not fully visualized in the form of bands because some are either overlapped with contiguous bands or present very low intensities. The spectra of amorphous Fo are clearly different; that is, they are based on single broad bands. In particular, the IR and Raman spectra of amorphous Fo present three and two well-defined zones, respectively: for IR, one band between 1000 – 800 cm^{-1}, a peak at about 600 cm^{-1} and another band between 500 – 300 cm^{-1}; for Raman, bands between 1000 –

800 cm^{-1} and between 700 – 400 cm^{-1}. These regions correspond essentially to the Si-O stretching and O-Si-O bending vibrations, respectively. However, vibrations associated with rotations of the SiO_4 tetrahedra and translations of Mg^{2+} also contribute in the low region of the lower bands. The significant broadening and blending of the IR bands presented by amorphous Fo compared to the crystal systems is due to the wider and more diverse distribution of bond lengths and angles given in the former system, which is typical in amorphous materials. In fact, the hyperfine structure of the IR spectra of amorphous Fo (built by bands consisting of single lines) present a great number of active vibrational bands that, upon imposing band width, overlap each other rendering squat-shaped bands. The presence of more active vibrational bands compared to the crystal system is mainly due to the lack of symmetry in amorphous Fo. This produces that some vibrations that are inactive in the crystal system by selection rules are active in the amorphous one. Moreover, the cell enlargement produces that equivalent vibrations by the translational symmetry in the minimal unit cell are different in the super cell, giving rise to the apparition of new vibrational bands. Astronomical IR and Raman measurements of cosmic silicates revealed that they are mainly in an amorphous state. The recorded spectra generally present two single broad bands at about 1000 cm^{-1} and 550 cm^{-1} associated with the Si-O stretching and O-Si-O bending vibrations, respectively [28]. Our simulated vibrational results of the amorphous Fo are thus in line with the astronomical IR and Raman spectral features.

As anticipated in Computational Methods, the reflectance spectrum of a given 3D-periodic system can be simulated with the CRYSTAL code. An important ingredient for the construction of the reflectance curves is ε_∞, whose values are discussed above. The B3LYP-simulated reflectance spectra of Fo, both crystalline and amorphous, are shown in Figure 7. The reflectivity is separated according to the three crystallographic axes (*a*, *b* and *c*), which for the crystal system are coincident with the vibration symmetry (B_{3u}, B_{2u} and B_{1u}, respectively). The topology of the simulated reflection curves of crystalline Fo perfectly matches with the experimental ones. A detailed analysis of the effect of different fitting procedures to properly reproduce the experimental reflectance spectra is provided in ref. [45]. The B3LYP-simulated reflectance spectra of amorphous Fo is significantly different. The broad reflectance curves of the crystalline system are sharper and present more bands. This is, in line to what is mentioned above, due to the more number of active vibrational modes in the amorphous systems.

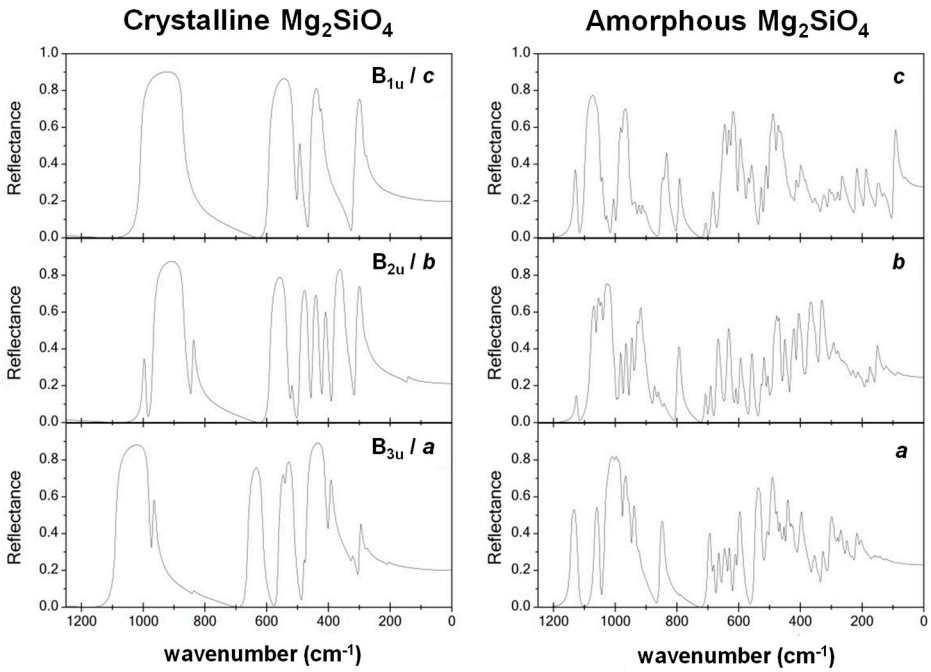

Figure 7. B3LYP-simulated Raman spectra of the crystalline and amorphous forsterite along the *a*, *b* and *c* directions.

Peer-reviewed version available at Minerals 2018, 8, 353; doi:10.3390/min8080353

3.2. Unit Cell Size Effects in the Amorphisation of the Mg_2SiO_4 System

This section reports the results related to the physico-chemical properties of amorphous Mg_2SiO_4 adopting different super-cell sizes; namely, 1×1×2, 2×1×2 and 2×2×2. The procedure to amorphize the corresponding crystalline systems was the same to that presented in the previous section; that is, classical MD simulations at 1800 K followed by B3LYP optimization of the resulting geometry to carry out the theoretical analysis. For all super-cell systems the Mg-Mg and Mg-O $g(r)$ pair correlation functions are similar, showing several broad but distinguishable bands representing the different Mg-Mg and Mg-O shells (see Figure S2 of SM). The similarity between the band widths of the different super-cell systems indicate that for all cases the amorphisation was definitely achieved.

The B3LYP-optimized structures of the different super-cell systems are shown in Figure 8, both in their atomistic and polyhedral forms. Table 6 presents the B3LYP-calculated lattice parameters, the range of the calculated Mg-O and Si-O bond lengths, the volume and the density of the bulk materials. In Table 3, the mean values and the associated deviations of the internal O-Si-O and O-Mg-O angles compared to the ideal values are also reported for the 2×1×2 and 2×2×2 systems. By visual inspection of the images of Figure 8, one can identify that the larger the super-cell size, the more distorted the tetrahedral SiO_4 and octahedral MgO_6 building blocks. This larger distortion is also reflected by the mean values and the average deviations of the internal angles. In the 2×1×2 and 2×2×2 super-cell systems they are larger than in the 1×1×2 one. In addition to this, a careful visual inspection of the atomistic structure of the amorphous systems, we realized that some "rare" structural motifs are present in the 2×1×2 and 2×2×2 systems, which are absent in the 1×1×2 one. In particular: i) pentacoordinated Si atoms (SiO_5 adopting a trigonal pyramid-like geometry), ii) pentacoordinated Mg atoms (MgO_5 adopting either square-pyramid- or trigonal pyramid-like geometries), and iii) tetracoordinated Mg atoms (MgO_4 adopting highly distorted tetrahedral geometries). These motifs are more common in the 2×2×2 super-cell systems than in the 2×1×2 one. The presence of these structural motifs is indicative that the degree of amorphisation is higher in these systems.

The calculated densities are reported in Table 6 and indicate that they decrease when the sizes of the super-cell increase; i.e., 3.373 g cm^{-3} (1×1×2) > 3.214 g cm^{-3} (2×1×2) > 3.172 g cm^{-3} (2×2×2). This is consistent with the fact that the larger the super-cell size, the larger the amorphous nature of the system. Indeed, by increasing the size of the super-cell, the structures can sport more defects and more porosity and consequently the density is lower. The calculated ε_∞ constants along the x, y and z directions (reported in Table 7) points out in the same direction. An increment of the super-cell size leads to a less dependency along the direction of the ε_∞ values as a consequence of the larger degree of disorder, which is equal along the three directions.

In relation to the vibrational properties, Figure 9 shows the simulated IR (a), Raman (b) and reflectance spectra (c). As mentioned above, the 1×1×2 system presents three and two well-defined broad IR and Raman bands, respectively. In contrast, the IR spectrum of the 2×2×2 system presents two largely broad bands; that is, the two bands in the low-frequency region of the 1×1×2 system overlap in the 2×2×2 system. Similar changes occur in the Raman spectrum, the two regions present in the 1×1×2 system become fused in the 2×2×2 system. The IR and Raman spectra of the 2×1×2 system present intermediate profiles between those of the 1×1×2 and the 2×2×2 systems. That is, the different frequency regions clearly identified in the 1×1×2 system are still identifiable but more diffusely. A similar transition in the topology of the reflectance spectra can be observed from the 1×1×2, 2×1×2 to the 2×2×2 systems. In this case, an increase of the unit cell size leads to spectra that present sharper and more bands due to the major number of independent active bands. All these changes in the topology of the vibrational-related spectra clearly indicate that there is a progressive increase of the amorphous nature from the 1×1×2 to the 2×2×2 super-cell systems.

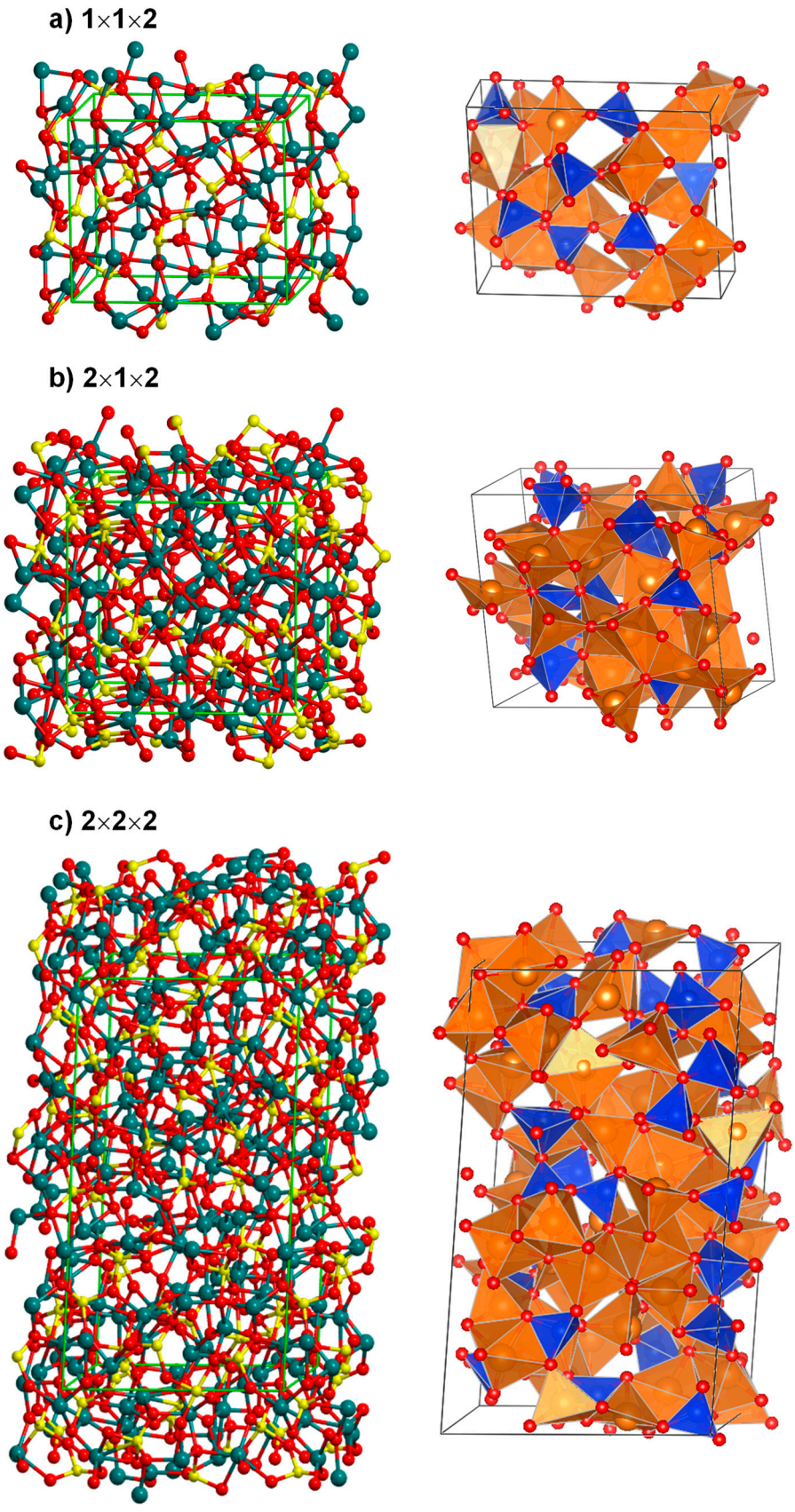

Figure 8. B3LYP-optimized structures of the bulk structures of Mg_2SiO_4 adopting the 1×1×2, 2×1×2 and 2×2×2 super-cells generated by classical MD simulations at T = 1800 K, both in the atomistic views (left) and in the polyhedral forms (right).

Peer-reviewed version available at Minerals 2018, 8, 353; doi:10.3390/min8080353

404 **Table 7.** Calculated high frequency dielectric constants (ε_∞) for the B3LYP-optimized 1×1×2, 2×1×2
405 and 2×2×2 Mg_2SiO_4 bulk structures along the *x*, *y* and *z* directions.

	1×1×2	2×1×2	2×2×2
$\varepsilon_{\infty,x}$	2.284	2.153	2.148
$\varepsilon_{\infty,y}$	2.247	2.161	2.135
$\varepsilon_{\infty,z}$	2.218	2.168	2.132

406

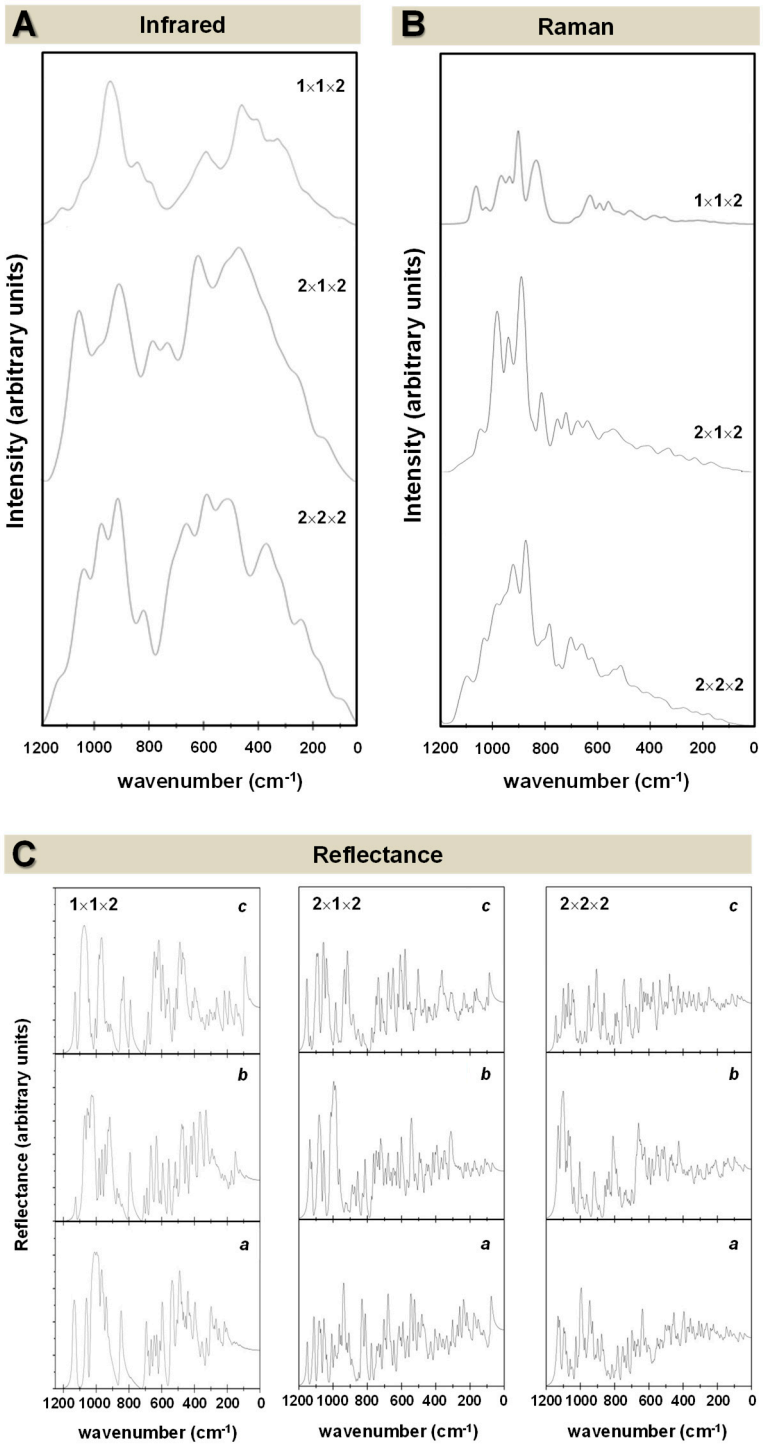

407 **Figure 9.** B3LYP-simulated Infrared (A) Raman (B) and Reflectance along the *a*, *b* and *c* directions (C)
408 spectra of the Mg_2SiO_4 bulk structures adopting the 1×1×2, 2×1×2 and 2×2×2 super-cells.

4. Conclusions

By combining classical MD simulations with periodic DFT calculations, a detailed theoretical study on the structural, dielectric and vibrational properties of Mg_2SiO_4 as a silicate test case has been presented. The amorphous structures for Mg_2SiO_4 have been generated using classical MD simulations at different temperatures within a melt and quench scheme tacking as the initial guess structure the crystalline phase. Periodic B3LYP calculations have been carried out to optimize the geometries of the generated structure and calculate their high frequency dielectric constants and simulate the IR, Raman and reflectance spectra. The most interesting points emerging from this work are:

- The Mg-Mg and Mg-O pair correlation functions g(r) derived from the classical MD simulations indicate that an increase of the temperature produces broader profiles of $g(r)$ indicating a progressive loss of crystallinity with temperature.
- B3LYP-optimized geometries of the amorphous bulk systems present larger distributions of bond lengths and angles than the crystal analogues due to the significant disorganization of the internal atomic positions. Consequently, the tetrahedral SiO_4 and octahedral MgO_6 motifs become largely distorted, which is characteristic of the amorphous materials. Calculated densities of the amorphous bulks are lower than the crystalline one due to the presence of internal cavities produced during the amorphisation process.
- Calculated high frequency dielectric constants along the x, y and z directions ($\varepsilon_{\infty,x}$, $\varepsilon_{\infty,y}$ and $\varepsilon_{\infty,z}$), while in the crystalline Mg_2SiO_4 they are clearly different in agreement with the direction dependency caused by the inherently crystallinity of the system, in the amorphous phases they are more similar, showing a convergence between the calculated $\varepsilon_{\infty,x}$, $\varepsilon_{\infty,y}$ and $\varepsilon_{\infty,z}$ values. Accordingly, ε_{∞} values do not depend on a particular direction because the system is likewise disordered in all the directions.
- While the IR and Raman spectra of the crystalline phase present well-defined narrow bands, the spectra of the amorphous-analogues, due to the wider and more diverse distribution of lengths and angles, are dominated by broader bands caused by multiple bands overlapping. The simulated spectra agree fairly well with those recorded for Mg_2SiO_4 in astrophysical environments. For the reflectance spectra, the broad reflectance curves of the crystalline system change by sharper and more bands for the amorphous systems, due to the presence of more number and active modes.
- In relation to the effect of the unit cell size, results provide clear evidence that an increase of the unit cell size infers a larger degree of amorphisation due to the presence of more internal degrees of freedom to be disordered.

Our results indicate that the combined approach of classical MD for structure evolution and quantum chemical DFT for electronic structure analysis is a reliable technique to investigate the physico-chemical properties of silicates.

Supplementary Materials: The following are available online, Figure S1: GULP-optimized structure for the bulk of the crystal Mg2SiO4. View of the unit cell (left), view of the extended periodic system (right), Figure S2: Mg-Mg (a) and Mg-O (b) pair correlation functions derived from the classical MD simulations for the 1×1×2, 2×1×2 and 2×2×2 systems. Table S1: Bond distance ranges of the (1×1×1) Mg_2SiO_4 bulk structures: experimental, GULP-optimized and B3LYP optimized values. Cell parameters and fractionary coordinates of the optimized systems.

Author Contributions: "Conceptualization, A.R.; Methodology, Software, Validation, Formal Analysis, Investigation, Resources, and Data Curation, J.A.M.-G. and J.N.-R; Writing-Original Draft Preparation, Writing-Review & Editing, and Visualization, J.A.M.-G. and A.R.; Supervision, Project Administration and Funding Acquisition, A.R.

Funding: This research was funded by MINECO (Projects CTQ2014-60119-P and CTQ2017-89132-P) and DIUE (Projects 2014SGR482 and 2017SGR1320).

Acknowledgments: A.R. is indebted to "Ramón y Cajal" program. J.A.M.-G is indebted to "Europa Excelencia" program, supported by CTQ2013-40347-ERC.

Conflicts of Interest: The authors declare no conflict of interest. The funders had no role in the design of the study; in the collection, analyses, or interpretation of data; in the writing of the manuscript, and in the decision to publish the results.

References

1. Rimola, A.; Costa, D.; Sodupe, M.; Lambert, J.-F.; Ugliengo, P. Silica Surface Features and Their Role in the Adsorption of Biomolecules: Computational Modeling and Experiments. Chem. Rev. 2013, 113, 4216-4313.
2. Fubini, B.; Otero Arean, C. Chemical Aspects of the Toxicity of Inhaled Mineral Dusts. Chem. Soc. Rev. 1999, 28, 373-381.
3. Fenoglio, I.; Prandi, L.; Tomatis, M.; Fubini, B. Free Radical Generation in the Toxicity of Inhaled Mineral Particles: The Role of Iron Speciation at the Surface of Asbestos and Silica. Redox Rep. 2001, 6, 235-241.
4. Otero Areán, C.; Barceló, F.; Fenoglio, I.; Fubini, B.; Llabrés i Xamena, F.X.; Tomatis, M. Free Radical Activity of Natural and Heat Treated Amphibole Asbestos. J. Inorg. Chem. 2001, 83, 211-216.
5. Turci, F.; Colonna, M.; Tomatis, M.; Mantegna, S.; Cravotto, G.; Gulino, G.; Aldieri, E.; Ghigo, D.; Fubini, B. Surface Reactivity and Cell Responses to Chrysotile Asbestos Nanofibers. Chem. Res. Toxicol. 2012, 25, 884-894.
6. Merget, R.; Bauer, T.; Küpper, H.; Philippou, S.; Bauer, H.; Breitstadt, R.; Bruening, T. Health Hazards due to the Inhalation of Amorphous Silica. Arch. Toxicol. 2002, 75, 625-634.
7. Hench, L.L.; Polak, J.M. Third-Generation Biomedical Materials. Science 2002, 295, 1014-1017.
8. Vallet-Regí, M.; Balas, F.; Arcos, D. Mesoporous Materials for Drug Delivery. Angew. Chem. Int. Edit. 2007, 46, 7548-7558.
9. Ceresoli, D.; Vanderbilt, D. Structural and Dielectric Properties of Amorphous ZrO_2 and HfO_2. Phys. Rev. B 2006, 74, 125108.
10. 1Zhao, X.; Ceresoli, D.; Vanderbilt, D. Structural, Electronic, and Dielectric Properties of Amorphous ZrO_2 from Ab Initio Molecular Dynamics. Phys. Rev. B 2005, 71, 085107.
11. Wang, Y.; Zahid, F.; Wang, J.; Guo, H. Structure and Dielectric Properties of Amorphous High-k oxides: HfO2, ZrO2, and their Alloys. Phys. Rev. B 2012, 85, 224110.
12. Madon, M.; Price, G.D. Infrared Spectroscopy of the Polymorphic Series (Enstatite, Ilmenite, and Perovskite) of $MgSiO_3$, $MgGeO_3$, and $MnGeO_3$. J. Geophys. Res. Solid Earth 1989, 94, 15687-15701.
13. Hofmeister, A.M. Single-Crystal Absorption and Reflection Infrared Spectroscopy of Forsterite and Fayalite. Phys. Chem. Miner. 1987, 14, 499-513.
14. Jäger, C.; Molster, F.J.; Dorschner, J.; Henning, T.; Mutschke, H.; L.B.F.M.Waters Steps toward interstellar silicate mineralogy IV. The crystalline revolution. Astron. Astrophys. 1998, 339, 904-916.
15. Henning, T.; Mutschke, H. Low-Temperature Infrared Properties of Cosmic Dust Analogues. Astron. Astrophys. 1997, 327, 743-754.
16. Fabian, D.; Jäger, C.; Henning, T.; Dorschner, J.; Mutschke, H. Steps toward interstellar silicate mineralogy V. Thermal evolution of amorphous magnesium silicates and silica. Astron. Astrophys. 2000, 364, 282-292.
17. Billinge, S.J.L.; Levin, I. The Problem with Determining Atomic Structure at the Nanoscale. Science 2007, 316, 561-565.
18. Tilocca, A. Current Challenges in Atomistic Simulations of Glasses for Biomedical Applications. Phys. Chem. Chem. Phys. 2014, 16, 3874-3880.
19. Umari, P.; Pasquarello, A. Infrared and Raman Spectra of Disordered Materials from First Principles. Diam. Relat. Mater. 2005, 14, 1255-1261.
20. Kroll, P. A DFT Study of Amorphous Silicon Oxynitride. J. Non-Cryst. Solids 2005, 351, 1127-1132.
21. Corno, M.; Pedone, A.; Dovesi, R.; Ugliengo, P. B3LYP Simulation of the Full Vibrational Spectrum of 45S5 Bioactive Silicate Glass Compared to v-Silica. Chem. Mater. 2008, 20, 5610-5621.
22. Karazhanov, S.Z.; Kroll, P.; Holt, A.; Bentzen, A.; Ulyashin, A. Comparative Analysis of Electronic Structure and Optical Properties of Crystalline and Amorphous Silicon Nitrides. J. Appl. Phys. 2009, 106, 053717.
23. Bondi, R.J.; Lee, S.; Hwang, G.S. First-Principles Study of the Mechanical and Optical Properties of Amorphous Hydrogenated Silicon and Silicon-Rich Silicon Oxide. Phys. Rev. B 2010, 81, 195207.
24. Lee, S.; Bondi, R.J.; Hwang, G.S. Ab Initio Parameterized Valence Force Field for the Structure and Energetics of Amorphous SiOx ($0 < x < 2$) Materials. Phys. Rev. B 2011, 84, 045202.

25. Berardo, E.; Pedone, A.; Ugliengo, P.; Corno, M. DFT Modeling of 45S5 and 77S Soda-Lime Phospho-Silicate Glass Surfaces: Clues on Different Bioactivity Mechanism. Langmuir 2013, 29, 5749-5759.
26. Landmann, M.; Köhler, T.; Rauls, E.; Frauenheim, T.; Schmidt, W.G. The Atomic Structure of Ternary Amorphous TixSi1−xO2 Hybrid Oxides. J. Phys. Condens. Matter 2014, 26, 253201.
27. Dovesi, R.; Orlando, R.; Erba, A.; Zicovich-Wilson, C.M.; Civalleri, B.; Casassa, S.; Maschio, L.; Ferrabone, M.; De La Pierre, M.; D'Arco, P.; Noël, Y.; Causà, M.; Rérat, M.; Kirtman, B. CRYSTAL14: A program for the ab initio investigation of crystalline solids. Int. J. Quantum Chem. 2014, 114, 1287-1317.
28. Henning, T. Cosmic Silicates. Annu. Rev. Astron. Astrophys. 2010, 48, 21-46.
29. Rubin, A.E. Mineralogy of meteorite groups. Meteorit. Planet. Sci. 1997, 32, 231-247.
30. Mumma, M.J.; Charnley, S.B. The Chemical Composition of Comets—Emerging Taxonomies and Natal Heritage. Annu. Rev. Astron. Astrophys. 2011, 49, 471-524.
31. Molster, F.; Kemper, C. Crystalline Silicates. Space Sci. Rev. 2005, 119, 3-28.
32. Vidali, G. H2 Formation on Interstellar Grains. Chem. Rev. 2013, 113 8762–8782.
33. Hama, T.; Watanabe, N. Surface Processes on Interstellar Amorphous Solid Water: Adsorption, Diffusion, Tunneling Reactions, and Nuclear-Spin Conversion. Chem. Rev. 2013, 113, 8783-8839.
34. van Dishoeck, E.F.; Herbst, E.; Neufeld, D.A. Interstellar Water Chemistry: From Laboratory to Observations. Chem. Rev. 2013, 113, 9043-9085.
35. Born, M.; Huang, K. Dynamical Theory of Crystal Lattices; Oxford University Press: Oxford, 1954.
36. Gale, J.D.; Rohl, A.L. The General Utility Lattice Program (GULP). Mol. Simul. 2003, 29, 291-341.
37. Roberts, C.; Johnston, R.L. Investigation of the Structures of MgO Clusters Using a Genetic Algorithm. Phys. Chem. Chem. Phys. 2001, 3, 5024-5034.
38. Flikkema, E.; Bromley, S.T. A New Interatomic Potential for Nanoscale Silica. Chem. Phys. Lett. 2003, 378, 622-629.
39. Hassanali, A.A.; Singer, S.J. Model for the Water−Amorphous Silica Interface: The Undissociated Surface. J. Phys. Chem. B 2007, 111, 11181-11193.
40. Becke, A.D. Density-Functional Thermochemistry. III. The Role of Exact Exchange. J. Chem. Phys. 1993, 98, 5648-5652.
41. Lee, C.; Yang, W.; Parr, R.G. Development of the Colle-Salvetti Correlation-Energy Formula into a Functional of the Electron Density. Phys. Rev. B 1988, 37, 785-789.
42. Civalleri, B.; D'Arco, P.; Orlando, R.; Saunders, V.R.; Dovesi, R. Hartree–Fock Geometry Optimisation of Periodic Systems with the Crystal Code. Chem. Phys. Lett. 2001, 348, 131-138.
43. Noel, Y.; Catti, M.; D'Arco, P.; Dovesi, R. The Vibrational Frequencies of Forsterite Mg_2SiO_4: An All-Electron Ab Initio Study with the CRYSTAL Code. Phys. Chem. Miner. 2006, 33, 383-393.
44. De La Pierre, M.; Orlando, R.; Maschio, L.; Doll, K.; Ugliengo, P.; Dovesi, R. Performance of Six Functionals (LDA, PBE, PBESOL, B3LYP, PBE0, and WC1LYP) in the Simulation of Vibrational and Dielectric Properties of Crystalline Compounds. The Case of Forsterite Mg_2SiO_4. J. Comput. Chem. 2011, 32, 1775-1784.
45. De La Pierre, M.; Carteret, C.; Orlando, R.; Dovesi, R. Use of Ab Initio Methods for the Interpretation of the Experimental IR Reflectance Spectra of Crystalline Compounds. J. Comput. Chem. 2013, 34, 1476-1485.
46. Noël, Y.; De La Pierre, M.; Maschio, L.; Rérat, M.; Zicovich-Wilson, C.M.; Dovesi, R. Electronic Structure, Dielectric Properties and Infrared Vibrational Spectrum of Fayalite: An Ab Initio Simulation with an All-Electron Gaussian Basis Set and the B3LYP Functional. Int. J. Quantum Chem. 2012, 112, 2098-2108.
47. Monkhorst, H.J.; Pack, J.D. Special Points for Brillouin-Zone Integrations. Phys. Rev. B 1976, 13, 5188-5192.
48. Pascale, F.; Zicovich-Wilson, C.M.; López Gejo, F.; Civalleri, B.; Orlando, R.; Dovesi, R. The Calculation of the Vibrational Frequencies of Crystalline Compounds and its Implementation in the CRYSTAL Code. J. Comput. Chem. 2004, 25, 888-897.
49. Zicovich-Wilson, C.M.; Dovesi, R.; Saunders, V.R. A General Method to Obtain Well Localized Wannier Functions for Composite Energy Bands in Linear Combination of Atomic Orbital Periodic Calculations. J. Chem. Phys. 2001, 115, 9708-9719.
50. Zicovich-Wilson, C.M.; Bert, A.; Roetti, C.; Dovesi, R.; Saunders, V.R. Characterization of the Electronic Structure of Crystalline Compounds through their Localized Wannier Functions. J. Chem. Phys. 2002, 116, 1120-1127.
51. Zicovich-Wilson, C.M.; Torres, F.J.; Pascale, F.; Valenzano, L.; Orlando, R.; Dovesi, R. Ab Initio Simulation of the IR Spectra of Pyrope, Grossular, and Andradite. J. Comput. Chem. 2008, 29, 2268-2278.

52. Ferrero, M.; Rérat, M.; Orlando, R.; Dovesi, R. The Calculation of Static Polarizabilities of 1-3D Periodic Compounds. The Implementation in the Crystal Code. J. Comput. Chem. 2008, 29, 1450-1459.
53. Ferrero, M.; Civalleri, B.; Rérat, M.; Orlando, R.; Dovesi, R. The Calculation of the Static First and Second Susceptibilities of Crystalline Urea: A Comparison of Hartree–Fock and Density Functional Theory Results Obtained with the Periodic Coupled Perturbed Hartree–Fock/Kohn–Sham Scheme. J. Chem. Phys. 2009, 131, 214704.
54. Maschio, L.; Kirtman, B.; Salustro, S.; Zicovich-Wilson, C.M.; Orlando, R.; Dovesi, R. Raman Spectrum of Pyrope Garnet. A Quantum Mechanical Simulation of Frequencies, Intensities, and Isotope Shifts. J. Phys. Chem. A 2013, 117, 11464-11471.
55. Carteret, C.; De La Pierre, M.; Dossot, M.; Pascale, F.; Erba, A.; Dovesi, R. The Vibrational Spectrum of CaCO3 Aragonite: A Combined Experimental and Quantum-Mechanical Investigation. J. Chem. Phys. 2013, 138, 014201.
56. Lacivita, V.; Erba, A.; Noël, Y.; Orlando, R.; D'Arco, P.; Dovesi, R. Zinc Oxide Nanotubes: An Ab Initio Investigation of their Structural, Vibrational, Elastic, and Dielectric Properties. J. Chem. Phys. 2013, 138, 214706.
57. Prencipe, M.; Maschio, L.; Kirtman, B.; Salustro, S.; Erba, A.; Dovesi, R. Raman Spectrum of $NaAlSi_2O_6$ Jadeite. A Quantum Mechanical Simulation. J. Raman Spectrosc. 2014, 45, 703-709.
58. Maschio, L.; Demichelis, R.; Orlando, R.; Pierre, M.D.L.; Mahmoud, A.; Dovesi, R. The Raman Spectrum of Grossular Garnet: A Quantum Mechanical Simulation of Wavenumbers and Intensities. J. Raman Spectrosc. 2014, 45, 710-715.
59. De La Pierre, M.; Carteret, C.; Maschio, L.; André, E.; Orlando, R.; Dovesi, R. The Raman Spectrum of CaCO3 Polymorphs Calcite and Aragonite: A Combined Experimental and Computational Study. J. Chem. Phys. 2014, 140, 164509.
60. Maul, J.; Erba, A.; Santos, I.M.G.; Sambrano, J.R.; Dovesi, R. In Silico Infrared and Raman Spectroscopy under Pressure: The Case of $CaSnO_3$ Perovskite. J. Chem. Phys. 2015, 142, 014505.
61. Schneider, A.G.; Schomborg, L.; Ulpe, A.C.; Rüscher, C.H.; Bredow, T. Structure, Vibrational Spectra and 11B-NMR Chemical Shift of $Na_8[AlSiO_4]_6(B(OH)_4)_2$: Comparison of Theory and Experiment. J. Phys. Chem. A 2016, 120, 7503-7509.
62. Ricca, C.; Grishin, A.; Ringuede, A.; Cassir, M.; Adamo, C.; Labat, F. Modeling Composite Electrolytes for Low-Temperature Solid Oxide Fuel Cell Application: Structural, Vibrational and Electronic Features of Carbonate-Oxide Interfaces. J. Mater. Chem. A 2016, 4, 17473-17482.
63. Zicovich-Wilson, C.M.; Pascale, F.; Roetti, C.; Saunders, V.R.; Orlando, R.; Dovesi, R. Calculation of the Vibration Frequencies of α-Quartz: The Effect of Hamiltonian and Basis Set. J. Comput. Chem. 2004, 25, 1873-1881.
64. Ferrero, M.; Rérat, M.; Kirtman, B.; Dovesi, R. Calculation of First and Second Static Hyperpolarizabilities of One- to Three-Dimensional Periodic Compounds. Implementation in the CRYSTAL Code. J. Chem. Phys. 2008, 129, 244110.
65. Ferrero, M.; Rérat, M.; Orlando, R.; Dovesi, R. Coupled Perturbed Hartree-Fock for Periodic Systems: The role of Symmetry and Related Computational Aspects. J. Chem. Phys. 2008, 128, 014110.
66. Dall'Olio, S.; Dovesi, R.; Resta, R. Spontaneous Polarization as a Berry Phase of the Hartree-Fock Wave Function: The Case of $KNbO_3$. Phys. Rev. B 1997, 56, 10105-10114.
67. Baranek, P.; Zicovich-Wilson, C.M.; Roetti, C.; Orlando, R.; Dovesi, R. Well Localized Crystalline Orbitals Obtained from Bloch Functions: The Case of $KNbO_3$. Phys. Rev. B 2001, 64, 125102.
68. Noel, Y.; Zicovich-Wilson, C.M.; Civalleri, B.; D'Arco, P.; Dovesi, R. Polarization Properties of ZnO and BeO: An Ab Initio Study through the Berry Phase and Wannier Functions Approaches. Phys. Rev. B 2001, 65, 014111.
69. Ferrari, A.M.; Valenzano, L.; Meyer, A.; Orlando, R.; Dovesi, R. Quantum-Mechanical Ab Initio Simulation of the Raman and IR Spectra of $Fe_3Al_2Si_3O_{12}$ Almandine. J. Phys. Chem. A 2009, 113, 11289-11294.
70. Maschio, L.; Ferrabone, M.; Meyer, A.; Garza, J.; Dovesi, R. The Infrared Spectrum of Spessartine: An Ab Initio All Electron Simulation with Five Different Functionals (LDA, PBE, PBESOL, B3LYP and PBE0). Chem. Phys. Lett. 2011, 501, 612-618.
71. Dovesi, R.; Pierre, M.D.L.; Ferrari, A.M.; Pascale, F.; Maschio, L.; Zicovich-Wilson, C.M. The IR Vibrational Properties of Six Members of the Garnet Family: A Quantum Mechanical Ab Initio Study. Am. Mineral. 2011, 96, 1787-1798.

72. Deer, W.A.; Howie, R.A.; Zussman, J. An Introduction to the Rock-Forming Minerals; 2nd ed.; Longman: London, 1992; p.^pp.
73. Servoin, J.L.; Piriou, B. Infrared Reflectivity and Raman Scattering of Mg_2SiO_4 Single Crystal. Phys. Status Solidi B 1973, 55, 677-686.
74. Iishi, K. Lattice dynamics of forsterite. Am. Mineral. 1978, 63, 1198-1208.
75. Chopelas, A. Single Crystal Raman Spectra of Forsterite, Fayalite, and Monticellite Am. Mineral. 1991, 76, 1100-1109.
76. Reynard, B. Single-Crystal Infrared Reflectivity of Pure Mg_2SiO_2 forsterite and $(Mg_{0.86},Fe_{0.14})_2SiO_4$ olivine. Phys. Chem. Miner. 1991, 18, 19-25.
77. Kolesov, B.A.; Geiger, C.A. A Raman Spectroscopic Study of Fe–Mg Olivines. Phys. Chem. Miner. 2004, 31, 142-154.
78. Hofmeister, A.M. Thermal Conductivity of Spinels and Olivines from Vibrational Spectroscopy: Ambient Conditions. Am. Mineral. 2001, 86, 1188-1208.
79. Sogawa, H.; Koike, C.; Chihara, H.; Suto, H.; Tachibana, S.; Tsuchiyama, A.; Kozasa, T. Infrared Reflection Spectra of Forsterite Crystal. Astron. Astrophys. 2006, 451, 357-361.
80. Suto, H.; Sogawa, H.; Tachibana, S.; Koike, C.; Karoji, H.; Tsuchiyama, A.; Chihara, H.; Mizutani, K.; Akedo, J.; Ogiso, K.; Fukui, T.; Ohara, S. Low-Temperature Single Crystal Reflection Spectra of Forsterite. Mon. Not. R. Astron. Soc. 2006, 370, 1599-1606.
81. Navarro-Ruiz, J.; Ugliengo, P.; Rimola, A.; Sodupe, M. B3LYP Periodic Study of the Physicochemical Properties of the Nonpolar (010) Mg-Pure and Fe-Containing Olivine Surfaces. J. Phys. Chem. A 2014, 118, 5866-5875.